Research article

Tapajyoti Das Gupta, Louis Martin-Monier, Jeremy Butet, Kuang-Yu Yang, Andreas Leber, Chaoqun Dong, Tung Nguyen-Dang, Wei Yan, Olivier J. F. Martin and Fabien Sorin*

Second harmonic generation in glass-based metasurfaces using tailored surface lattice resonances

Abstract: Dielectric metasurfaces have shown prominent applications in nonlinear optics due to strong field enhancement and low dissipation losses at the nanoscale. Chalcogenide glasses are one of the promising materials for the observation of nonlinear effects thanks to their high intrinsic nonlinearities. Here, we demonstrate, experimentally and theoretically, that significant second harmonic generation (SHG) can be obtained within amorphous Selenium (Se)-based chalcogenide metasurfaces by exploiting the coupling between lattice and particle resonances. We further show that the high-quality factor resonance at the origin of the SHG can be tuned over a wide wavelength range using a simple and versatile fabrication approach. The measured second harmonic intensity is orders of magnitude higher than that from a dewetted Se film consisting of random Se nanoparticles. The achieved conversion efficiency in the resonance region is of the order of 10^{-6} which is comparable with direct bandgap materials and at least two orders of magnitude higher than that of conventional plasmonics- and Si-based structures. Fabricated via a simple and scalable technique, these all-dielectric architectures are ideal candidates for the design of flat nonlinear optical components on flexible substrates.

Keywords: chalcogenide glass; large area fabrication; metasurface; second harmonic generation; surface lattice resonance.

1 Introduction

High refractive index dielectric metasurfaces [1–4] are sub-wavelength nanostructured arrays that provide a promising alternative to plasmonic structures [5, 6], especially thanks to their intrinsic low dissipation losses [2], multipolar resonances [7], and their inherent magnetic response. An important application of such dielectric resonators lies in nonlinear optics [7]. In particular, second harmonic generation (SHG) has thus far mainly relied on III–V semiconductors [8, 9] due to their non-centrosymmetric crystalline structures. Other common candidates include silicon [10], plasmonic-based metasurfaces [11, 12], and hybrid structures [13] which have all shown a strong SHG enhancement as compared to their thin films counterpart.

Second harmonic (SH) signals can also be strongly enhanced by using properly engineered resonances. For example, resonators with broken symmetry [8, 14] have proven efficient to produce high-quality factor (QF) resonances and hence strong field enhancement at both the fundamental and the SH wavelengths. Other approaches lie in the fabrication of high aspect ratio pillar-like structures [15], where the so-called bound state in continuum allows for a high QF using single pillar structures. Similar high efficiency has also been reported in plasmonic architectures, for example with complex metal-dielectric-metal (MDM) cavities relying on patch antennas [16] or chiral structures [17]. These interesting designs nevertheless require a high aspect ratio or sophisticated shapes, thus involving complex e-beam processes, which limits the applicability of such devices.

*Corresponding author: Fabien Sorin, Ecole Polytechnique Federale de Lausanne, Lausanne, VD, Switzerland,
E-mail: fabien.sorin@epfl.ch
Tapajyoti Das Gupta, Indian Institute of Science, Bangalore, 560012, India. https://orcid.org/0000-0002-4605-2071
Louis Martin-Monier, Jeremy Butet, Kuang-Yu Yang, Andreas Leber, Chaoqun Dong and Olivier J. F. Martin, Ecole Polytechnique Federale de Lausanne, Lausanne, VD, Switzerland
Tung Nguyen-Dang, Center for Polymers and Organic Solids, University of California Santa Barbara, Chemistry Building, Room 3132, Santa Barbara, CA, 93106-9010, USA
Wei Yan, MIT, 77 Massachusetts Ave, Cambridge, MA, 02139-4307, USA

Another way to engineer high QF metasurfaces is to use surface lattice resonances. For a bare lattice made from nonresonant particles, near-field enhancement is observed at the Rayleigh-anomaly wavelength [18, 19]. This resonance spectral position is defined by:

$$\lambda_{(i,0)} = a_0 \cdot \left(\frac{n}{|i|} - \frac{\sin\theta}{i} \right), \tag{i}$$
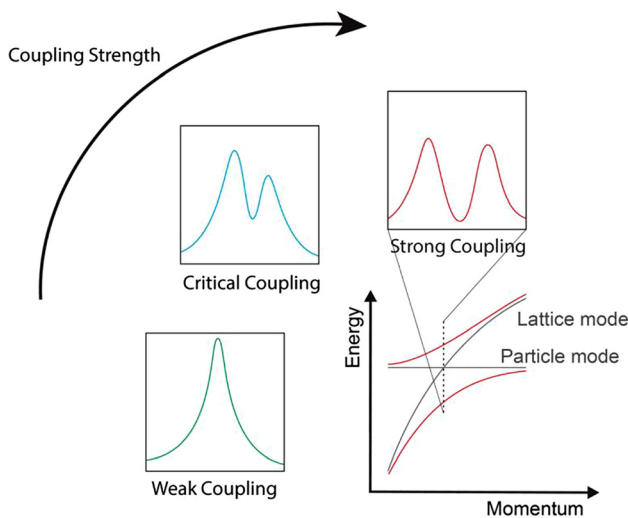
where a_0 is the periodicity or the lattice constant of the arrays, n is the surrounding refractive index, θ is the angle of incidence, and i is an integer denoting the diffraction order. Under normal incidence, this resonance is hence solely dependent on the lattice periodicity and the surrounding refractive index [20]. By additionally considering resonant nanoparticles, a wealth of optical phenomena and spectral features can be exploited by relying on the coupling between lattice and Mie-type modes associated with the particle [21], as illustrated in Figure 1.

For weak coupling, both resonances are barely modified and the response of the system remains essentially Lorentzian. When coupling reaches the critical regime, this interaction leads to the emergence of a high QF Fano-type resonance [22–24]. The particle size and periodicity control the coupling strength. When it reaches the critical regime, the coupling losses exactly balance the intrinsic losses and the energy stored in the system reaches its maximum [23]. This corresponds to a high QF

Figure 1: The optical response of a system that supports both lattice and particles modes can be tuned by adjusting the coupling between both modes. Weak coupling leads to a Lorentzian response (green spectrum), critical coupling produces a Fano-type line shape (blue), while the response of the system exhibits two symmetric peaks in the strong coupling regime (red). These two peaks correspond to the energy splitting associated with the avoided crossing between the lattice and particle modes.

Fano-type resonance with the strongest near-field enhancement, thus the strongest nonlinear light generation. A strong coupling regime further leads to an energy splitting yielding two characteristic peaks [25]. Interestingly, the entire response of the system can be controlled by the interactions between the particle resonance (determined by its material composition and shape) and the lattice resonance, which is governed by the array periodicity and the surrounding refractive index [26, 27]. Simple geometrical handles such as lattice periodicity or interparticle gap (equivalent to particle size for a fixed period) allow for tunable coupling between particle and lattice modes. The resonator shape or constituting materials further represent additional degrees of freedom. Engineering strong resonance through engineered mode coupling proves a versatile platform for light–matter interaction at the nanoscale, and in particular for enhancing SHG emission [28].

However, independent control over geometrical parameters commonly relies on time and cost-intensive lithographic techniques and thus fails to optimize the nanostructures for enhanced SH performance. Previous works have proposed simple techniques to controllably tune a single geometrical parameter without relying on lithographic techniques, for example using thermoplastics [29], stretched polydimethylsiloxane (PDMS) during the nano-imprinting process [30], or using elastomeric PDMS [31] as a substrate. By either using a constant particle size or constant lattice period, these works provided a single geometrical handle to control mode coupling. A simple and versatile way to independently tune two or more geometrical parameters remains to be developed.

Here, we address this issue and demonstrate a novel materials and fabrication platform for high conversion efficiency SH dielectric nanostructures from the coupling between particle resonance with lattice resonance, via the template dewetting of chalcogenide glasses-based metasurfaces. Chalcogenides [32–36] are ideal dielectric material for nonlinear photonics because of the ability to precisely tailor their optical properties by tailoring their composition, the noncentrosymmetry of the crystalline structure of some composition such as pure crystalline Selenium (Se), and their amenability to be nanostructured in various architectures [37, 38], yet they have been seldom used due to a lack of suitable resonance engineering strategy, and versatile materials processing approach. The process we developed [39] enables tuning independently the lattice period (through imprinting pressure) and the particle size or diameter (through successive dewetting) to understand and optimize the emergence of Fano-type surface lattice resonance. With this fabrication flexibility,

coupling between the diffractive lattice and the radiative particle modes can be properly controlled, which is subsequently exploited to enhance the SH signal. We observe an enhanced SHG at the Fano-type surface lattice resonance of two orders of magnitude larger than the nonresonant region and four orders of magnitude higher compared to unstructured thin films. The SH conversion efficiency we observe is of the order of 10^{-6}, which outperforms conventional plasmonics and Si-based structures [10] and is at par with direct bandgap semiconductor materials [8, 9]. This experimental effect is investigated through finite-difference time-domain (FDTD) simulations by relating the origin of the strong SHG to the field enhancement induced by critical coupling between the lattice and radiative modes. The design methodology and SH efficiency reported in this article pave the way for nonlinear chalcogenide-based light sources using a highly scalable and versatile fabrication platform.

2 Experimental

2.1 Sample fabrication technique

The sample fabrication process starts with the fabrication of our master mold. To achieve the master mold, an array of inverted pyramids with a 350 nm period was obtained by interference lithography followed by KOH anisotropic etching on p-doped Si [100] wafer (CEMITEC, Spain). Using a negative PDMS stamp (Sylgard 184, Dow Corning, USA), the Si microstructure was reproduced via nanoimprinting onto a thermoplastic polycarbonate (PC) sheet (Goodfellow, UK). The thin chalcogenide film (ChG) was then deposited by thermal evaporation (UNIVEX 250, Oerlikon, Germany). Annealing was achieved on a hot plate (Isotemp Fisher Scientific) (80 ℃) to induce thermal dewetting (Figures S.I.1 and 2).

2.2 Scanning electron microscope characterization and analysis

All scanning electron microscope (SEM) samples were coated with a 10 nm carbon film. The SEM images were taken with a Zeiss Merlin field emission SEM equipped with a GEMINI II column operating at 3.0 kV with a probe current of 120 pA. All SEM image analyses were done using Image J software, averaging the measures over a large number N of particles for the size distribution ($N > 100$) and a reduced number of periods P for the period extraction ($p > 5$).

2.3 Simulations

The linear simulations were performed using the commercially available FDTD software Lumerical. The optical constants were obtained experimentally via spectroscopic ellipsometry (Sopra GES 5E) analysis of thin film of selenium (Figure S.I.3). A linearly polarized plane wave source was used for all the simulations. The substrate index was chosen to be 1.6, which is the average index of PC [40]. Periodic boundary conditions were used in the transverse direction and a perfectly matched layer was used in the wave propagation direction. The particle is defined as the overlap between an ellipsoid with in-plane radius r and conical shape of base length d (Figure S.I.4). The ellipsoid in-plane radius r is defined as $r = d(1 + \sqrt{2})/2$, while the ellipsoid center coincides with the pyramid base center. The particle radius in this work refers to the ellipsoid radius in the model. The height of the pyramid shape was kept fixed at 200 nm. For the electric field amplitude spectral evolution, a time monitor was placed in the interparticle gap i.e. in between two neighbor ellipsoids as well as in the center of the ellipsoidal particle. For magnetic field amplitude spectral evolution, a time monitor was placed at the particle center (i.e. the ellipsoid center). For the maximal electric field enhancement calculation, the value of the maximal field intensity was extracted from the electric field distribution map at the corresponding resonance wavelength, within the metasurface's symmetry plane. Additional calculations based on the Mie theory were performed to determine the resonance conditions for Se particles as a function of their radius (Figure S.I.5).

### 2.4 Linear and nonlinear measurements

The linear transmission spectra were measured using an integrating sphere coupled with a spectrometer (Ocean Optics, UV–Vis USA). For the nonlinear optical measurements, a commercial multiphoton scanning microscope (LEICA SP5MULTI-PHOTON) combined with a 20×/1.00 NA water-immersion objective (HCX PL APO) and a Ti:Sapphire femtosecond laser (Chameleon ultra-laser, repetition rate: 80 MHz, operating wavelength $\lambda = 800$ nm, pulse duration: 140 fs) having a beam diameter of 20 μm combined with an electro-optical modulator to adjust the input power was used. The backward scattered SHG from the structures was collected by the same objective followed by a beam splitter, a band-pass filter (of different wavelengths with a bandwidth of 10 nm), and a photomultiplier tube (NDD PMT). The XY scanner (400 Hz scanning speed) of the microscope enabled a 387.5 μm × 387.5 μm field range with 758.32 nm pixel resolution at 800 nm. For the wavelength dependency of SHG, the incident laser power on the sample was measured using a power meter and was kept at 3 mW. The quadratic dependence between the SH intensity and the input power was recorded carefully tuning the input power. The estimated incident power for the quadratic dependency is shown in Supplementary information in S.I.9.

3 Results and discussion

3.1 Fabrication of metasurfaces

The fabrication process is schematized in Figure 2a and is detailed in the experimental section (Fabrication technique) [39]. The obtained pattern is illustrated in the SEM images in SI (Figure S.I.1).

We start by investigating a simple, yet thus far unexplored, approach to tailor the lattice period of the underlying pattern, via engineering the applied pressure
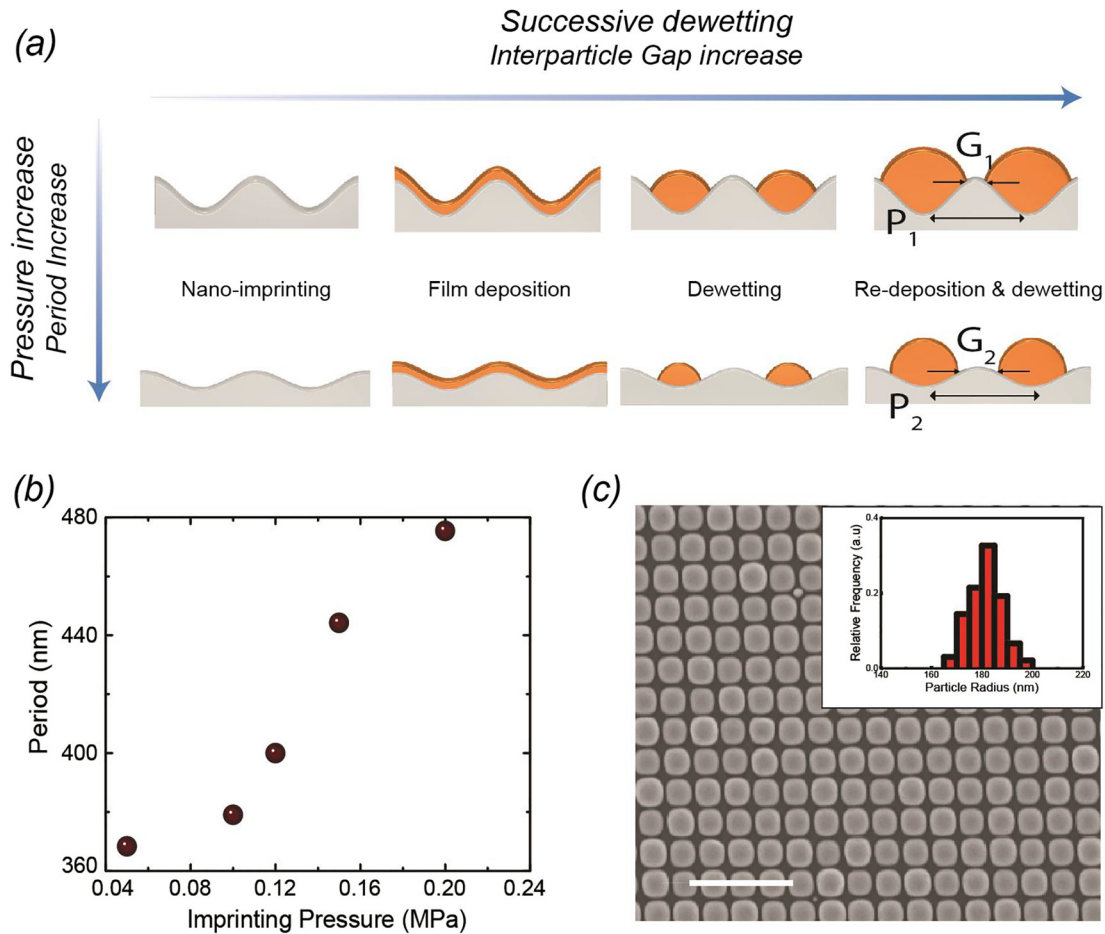
Figure 2: Fabrication process of the metasurfaces.
(a) Schematic diagram illustrating the process of fabrication. (b) Variation of the periodicity with the applied pressure. (c) Scanning electron microscopy image of dewetted Se nano-arrays obtained by successive dewetting corresponding to a total cumulative thickness of 60 nm for a fixed periodicity of 400 nm. The scale bar is 2 μm. The graph in the inset shows the particle size distribution. A Gaussian fit provides an average radius value $r = 181 \pm 13$ nm.

during the imprinting step. Figure 2(b) shows the change in the period on a bare PC textured sample when the pressure varies from 0.05 to 0.2 MPa (Figure S.I.1). As the applied pressure during the nanoimprinting process is increased, we observe an increase in the period. The SEM images (see SI Figure S.I.1) suggest a well-controlled increase of the array periodicity with the applied pressure, which will be later exploited to tune the lattice resonance.

On the other hand, our process also proposes a way to control Se particle size or radius (or equivalently their spacing distance, labeled G in this work). By successively depositing and dewetting thin layers of Se of controlled thickness, it is possible to control the inter-particle distance down to approximately 10 nm (Figure S.I.2) while increasing the particle size.

Controlling evaporated thickness hence provides a handle over the interparticle gap. As apparent in Figure 2(c),

there is an inherent size distribution for dewetted particles. This size distribution is intricately linked to a number of factors including substrate inter-pyramid spacing, local substrate curvature, and film thickness. Interestingly, the particle size distribution can be narrowed down by reducing the interparticle gap (equivalent to increasing the particle size), independently of the factors cited above. This point has already been extensively investigated in reference [39], and we refer the reader to this work for more details. The particles shown in Figure 2(c) have a radial distribution of $r = 181 \pm 13$ nm, which suggests a high degree of order. Reduced ordering proves detrimental to the resonance sharpness, characterized by the full width half maximum (FWHM). The sharpness of the resonances experimentally obtained in this work further supports that the high degree of order is maintained for the considered range of particle sizes and periods.

Note that the Se particles must be tailored to support resonances at wavelengths longer than the spectral absorbing region of amorphous Se (non-negligible losses below 600 nm, see Figure S.I.3) and within the spectral range of our Ti: sapphire femtosecond laser (λ = 650–1200 nm). The computed single-particle scattering spectra (Figure S.I.5) show broad resonances, indicating that a particle size of radius above 300 nm is a prerequisite to have a resonance inducing a strong field enhancement at approximately 700 nm.

3.2 Tunable optical properties

3.2.1 Linear optical properties

Figure 3(a) shows the change in the experimental transmission spectrum when we fix the lattice period P and vary the particle size $S = 2r = P - G$ by the process of successive dewetting, where r is defined as the radius of the particle. The total deposited thicknesses represented in the graph (40, 50, and 60 nm) dictate the size of the particles and therefore also their spacing. The initial broad dip for 40 nm thickness decouples into two dips, which redshift as the thickness (and hence the size of the particles) increases, indicative of a change in the coupling regime as the particles resonance shift, as illustrated in Figure 1. Before investigating and exploiting this effect, we experimentally study the effect of changing the lattice period P, while keeping the same deposition conditions (60 nm film thickness). As shown in Figure 3(b), it reveals the

appearance of a strong asymmetric resonance, which increases when P is varied from 360 to 400 nm. A further increase of the period to 450 nm leads to spectral reshaping from one asymmetric Fano-type resonance to two symmetric resonances, indicative of a change in the coupling strength in the system [21]. From these experimental results, we identify a sharp resonance of FWHM of approximately 4 nm in the air for a lattice period of 400 and 60 nm total thickness.

To unveil the origin of the different resonances and their coupling, FDTD simulations were performed using the commercially available Lumerical software. The effect on the transmission spectrum of decreasing the interparticle gap upon successive dewetting is first illustrated in Figure 4(a), keeping a fixed period p = 400 nm. The interparticle gap distance was varied from 50 to 10 nm. The simulated transmission spectra (Figure 4(a)) show a sharp asymmetric dip that red-shifts on decreasing the interparticle gap, which corresponds to experimental observations. Figure 4(b) and (c) relate the respective spectral evolution of the electric field amplitude in the interparticle gap and the magnetic field amplitude at the particle center. The interparticle electric field maximum both decreases and red-shifts with a reduced interparticle gap (Figure 4(b) and (d)). This electric field maximum is attributed to the interference of the electric dipole (ED) mode and the diffraction order due to the lattice (LR) as observed from the electric field maps (ED-LR, Figure S.I.6). The evolution in Figure 4(b) corroborates the trend observed for maximal electric field intensity at resonance in the metasurface's symmetry plane (Figure 4(d)), which strongly decreases as
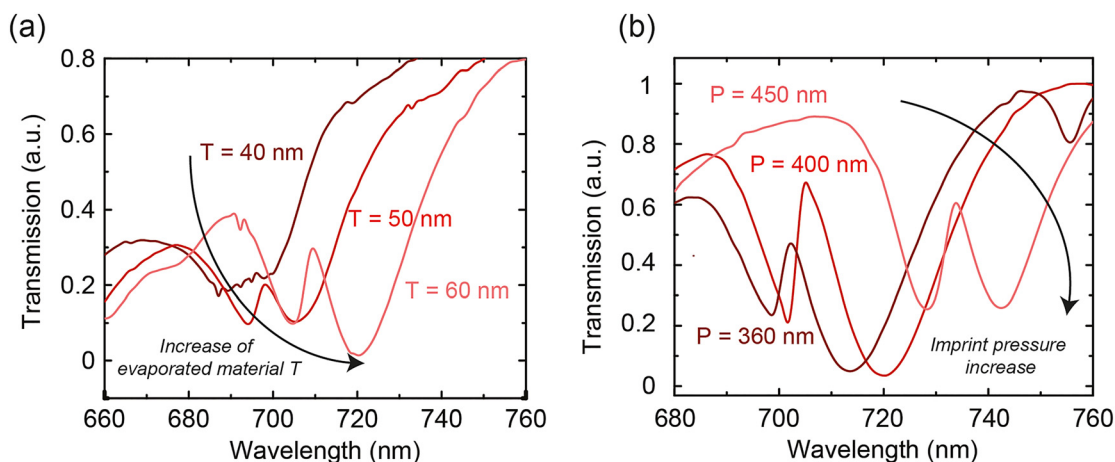
Figure 3: Experimental transmission spectra illustrating the gap and the lattice effect.
(a) Transmission spectra were obtained for successive dewetting steps corresponding to an increased equivalent thickness T, maintaining the pressure during the nanoimprint at 0.1 MPa. The transmission spectrum is observed to split from a single broad resonance (at 40 nm) to two resonances (50 and 60 nm). (b) Transmission spectra for a 60 nm deposited film obtained as the pressure during the imprinting process are varied from 0.1 to 0.2 MPa. As the nanoimprinted pressure is increased, the asymmetric resonance becomes sharper (0.15 MPa) corresponding to an increase in lattice periodicity to 400 nm. Further increases of the pressure lead to the disappearance of Fano resonance and give rise to two broad symmetric dips (period 450 nm).

the gap is reduced from 50 to 10 nm. This effect contrasts with the appearance of hot spots at a lower gap in plasmonic metasurfaces [41, 42]. As shown in Figure 4(c), the magnetic field monitor (at the particle center) indicates a broad magnetic resonance (MD) associated with the particle, which overlaps with another sharper magnetic peak, located at the exact position of the ED-LR. The origin of the MD mode is associated with Mie-type modes due to the ensemble (periodic arrays) macroscopic resonant response which is excited with a circular flow of the displacement current (Figure S.I.6). The spectral position of such MDs can be tuned by changing the size as well as their arrangement of particles employed for meta-atoms [1–3]. Depending on the particle diameter (and thus the gap G) the two modes change spectral shape – from a Fano-type resonance (particle gap 50 nm) to a more symmetric resonance (particle gap 10 nm). Such spectral tuning directly relates with the critical and strongly coupled regime as we explain schematically in Figure 1. Figure 4 shows that both the particle as well as the lattice modes varies with the change in the particle size (G) or lattice constant (P). This behavior is expected as schematically shown in Figure S.I.7, for one specific value of G and P, a particular lattice and particle mode (Figure S.I.7(a)). A change in G leads to a change in the particle mode (particle mode 2 Figure S.I.7(b)) and hence a change in the interaction, thus leading to a change in the entire spectrum. A similar effect arises when the lattice is varied while the particle size is fixed as suggested in Figure S.I.7(c) and visible in Figure 4.

Our simulations clearly suggest that MD and ED-LR modes interfere with the considered range of interparticle gaps.

We now turn toward the influence of the array periodicity on the optical spectrum, keeping a fixed particle size $S = P - G = 350$ nm. Structures with varying lattice periods (from 370 to 450 nm, see Figures 4(e)–(g)) are illuminated with a polarized plane wave at normal incidence. The sharp asymmetric resonance apparent in the transmission spectrum (Figure 4(e)) for an initial small period increases in strength and then transforms to a symmetric dip for the highest periodicities considered in this work (450 nm). As the period increases to 600 nm (Figure S.I.8), the two resonances merge, leading to a single resonance, which disappears upon increasing the period to 800 nm. The asymmetric resonance observed in the experimental (Figure 3(a)) and simulated (Figure 4(e)) transmission spectra for a small period, is mainly attributed to the ED-LR (Figure S.I.6). Figure 4(f) and (g) show the electric and magnetic field amplitude at the interparticle gap and particle center, respectively, as the array period is varied from 370 to 450 nm. The interparticle electric field

maximum (associated with the ED-LR as shown in Figure 4(f)) first increases with an increase in the period from 370 to 410 nm and decreases when the period is further expanded beyond 410 nm. This is in line with the trend observed for maximal electric field intensity at resonance, based on the electric intensity profile distribution in the metasurface's symmetry plane (Figure 4(h) and (i)), which reaches a maximal value at around 400 nm. For decreasing periods below 400 nm, the ED-LR and MD modes couple critically giving rise to a sharp Fano resonance, with the highest QF of 175. On increasing the array period, we observe the modes to shift toward the red and the Fano resonance becomes more symmetric with an observed increase of the FWHM and lower QF. This appearance of symmetric modes is an indication of a strong coupling regime (Figure 1) between ED-LR and MD modes as suggested in Figure 4(e)–(g). This symmetric mode with a lower QF leads to a sharp drop in the field enhancement [20, 42] above a period of 430 nm (Figure 4(g)).

Thus, to obtain a high QF it is essential to engineer the mode coupling through the fine tuning of the lattice period and particle size allowed by our process. For this specific substrate, texture, and dielectric material, we find that the optimal resonance overlap occurs at $\lambda = 700$ nm for a lattice period of 400 nm and a Se particle size of 350 nm. This architecture leads to sharp resonant modes with a strong field enhancement and a high experimental QF of 175 at $\lambda = 700$ nm.

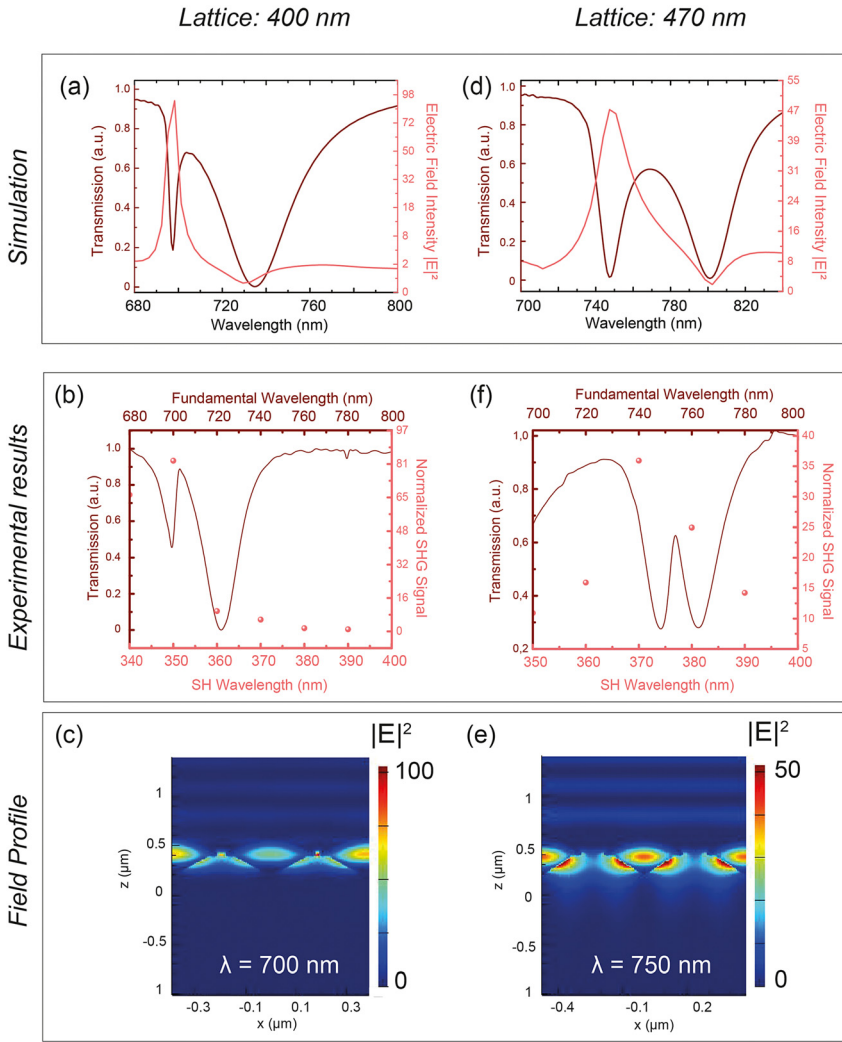### 3.2.2 Second harmonic generation

To demonstrate the potential of our metasurfaces design capabilities, we used the previously demonstrated nanophotonic structures with optimized light–matter interactions for resonantly enhanced SHG. Simulated linear transmission spectrum (Figure 5(a), wine-red curve) for a nanoparticle size of 350 nm and a period of 400 nm reveals a dip associated with the lattice resonance excitation. The experimental linear measurement is in line with simulation predictions, showing a corresponding dip in transmission at $\lambda = 700$ nm (Figure 5(b), wine-red curve). This resonance leads to an enhancement of the electric field intensity by two orders of magnitude (~90×) in comparison with off-resonance spectral regions (Figure 5(b), light red markers).

SHG measurements were performed in reflection using a previously reported setup [43]. From each of the obtained scanned images, the SH intensity at a particular wavelength was calculated from the mean value of those images as shown in Figure 5(c) (light red dots) when the pump wavelength is tuned between $\lambda = 680$ and 780 nm. The conversion efficiency η is defined as:
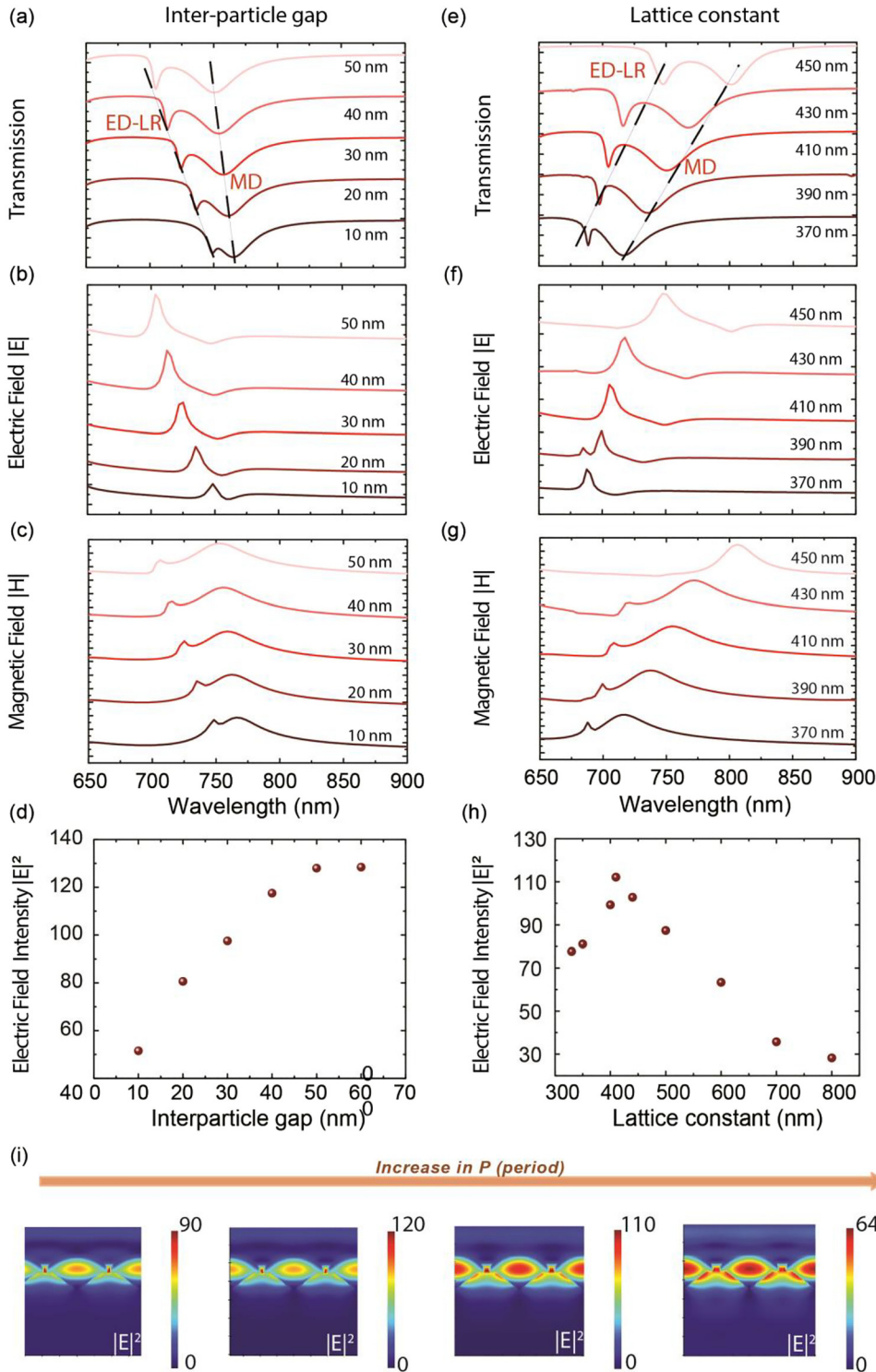
Figure 4: Effect of the periodicity and gap on the mode properties.
(a)–(d) Effect of gap/particle size for a period of 400 nm. (a) Simulated transmission spectra, (b) simulated electric field magnitude in the interparticle region, and (c) simulated magnetic field magnitude at particle center as a function of wavelength with a reduction of the interparticle gap from 50 to 10 nm. (d) Simulated maximal electric field intensity along the unit period's symmetry plane. (e)–(h) Effect of periodicity for a fixed particle diameter of 350 nm. (e) Simulated transmission spectra, (f) simulated electric field magnitude in the interparticle region, and (g) simulated magnetic field magnitude at particle center as a function of wavelength with an increase in the period from 370 to 400 nm. (h) Simulated maximal electric field intensity along the unit period's symmetry plane. (i) Simulated field distribution in increasing lattice constant.

Lattice: 400 nm *Lattice: 470 nm*

Figure 5: Resonantly Enhanced Second Harmonic Generation in critically and strongly coupled conditions.
(a)–(c) Fixed period of 400 nm and particle size of 350 nm, providing critical coupling conditions. (a) Simulated linear transmission spectrum (wine-red) and electric field intensity evaluated at the Se nanoparticle center (light red). (b) Experimental transmission spectrum (wine-red curve) and normalized second harmonic signal (with respect to the incident power, in light red dots) showing a ~90× signal enhancement. (c) Distribution of the electric field intensity enhancement in a plane perpendicular to the metasurface for an incident wavelength $\lambda = 700$ nm. (d)–(f) Fixed period of 470 nm and particle size of 350 nm, yielding a strongly coupled regime. (d) Simulated linear transmission spectrum (wine-red) and electric field intensity evaluated at the Se nanoparticle center (light red). (e) Experimental transmission spectrum (wine-red curve) and normalized second harmonic signal (with respect to the incident power, in light red dots) showing a ~38× signal enhancement. (f) Distribution of the electric field intensity in a plane perpendicular to the metasurface for an incident wavelength $\lambda = 750$ nm.

$$\eta = \frac{P^{SH}_{photon}}{\left(P^{Fundamental}_{photon}\right)} \tag{ii}$$

where P^{SH}_{photon} and $P^{Fundamental}_{photon}$ are the power of the generated SH and the fundamental incident signal, respectively. The intensity I is related to the power P according to the following equation:

$$I(\lambda) = \int P \cdot dA = nh\frac{c}{\lambda} \tag{iii}$$

where A is the area of illumination (defined by the LASER beamwidth of 20 μm). We proceed to measure the

re-emitted SH intensity P_{SH} over a fixed integration time (10 s), as well as the power of the fundamental $P_{Fundamental}$ reflected from a gold mirror surface over a reduced integration time to avoid saturation (1 s).

We proceed to measure the re-emitted SH intensity I_{SH} over a fixed integration time (10 s), as well as the intensity of the fundamental $I_{Fundamental}$ reflected from a gold mirror surface over a reduced integration time to avoid saturation (1 s). All measurements are done under normal incidence. Normalizing these powers with time and combining relations (ii) and (iii) finally provide the conversion

efficiency, which is evaluated here at 10^{-8} at $\lambda = 800$ nm (off-resonance). The normalized SHG power shows a peak at the asymmetric electric resonance ($\lambda = 700$ nm) due to the electromagnetic field enhancement (Figure 5(a)). When exciting at the resonant wavelength of $\lambda = 700$ nm (i.e. maximal field enhancement), the SH signal normalized with the incident power exhibits a 100 times enhancement with respect to the nonresonant region ($\lambda = 800$ nm), and almost four orders of magnitude enhancement as compared to the nonpatterned Se dewetted film of comparable thickness in the nonresonant region ($\lambda = 800$ nm) (Figure S.I.9). The SH enhancement is thus attributed mainly to the electric-dipole lattice resonance (EDLR) mode, while a lower SH signal was obtained at MD mode. From the field simulation (Figure S.I.6) it is apparent that the MD enhancement is located within the particle as compared to the surface located EDLR mode. This field localization at MD resonance within such amorphous structures leads to significant low SH enhancement clearly demonstrating the surface effect of SH enhancement in such amorphous Se-based metasurface.

Moreover, our meta-structures do not show a clear influence of incident light polarization on the conversion efficiency. Rotating the incident light polarization by 90° changes the emission efficiency at $\lambda = 350$ nm from 90× to about 60× as compared to the nonresonant region (Figure S.I.11), which is mainly attributed to the small asymmetry in the nanoimprinted structure (Figure S.I.1). This leads to a reduction in the coupling strength and hence a reduction in the field enhancement.

Figure 5(d)–(c) reproduce the study done for Figure 5(a)–(c) for an increased period of 470 nm with the same particle size of 350 nm. Based on the transmission spectrum, this situation is akin to the strong coupling illustrated in Figure 1 and demonstrates comparatively broader symmetric resonances with lower QF and field enhancement and SHG emission as compared with the critically coupled case of Figure 5(a)–(c).

The dependence of the field intensity enhancement ($I_\omega = |E|^2$) on the lattice period (P) for these structures follows a quadratic law defined by:

$$I_\omega = A_o P^{-2}, \tag{iv}$$

where A_o is determined by the nature of meta-atoms and metasurface design (see S.I. Figure S.I.12(a)). It is worth noting that a similar quadratic dependency on critical coupling has been observed for asymmetric structures [44]. Furthermore, the FWHM is also observed to scale

quadratically with the lattice period based on numerical simulations (S.I. Figure S.I.12(b)):

$$\mathbf{FWHM} = B_o |P - P_c|^{-2} \tag{v}$$

where B_o is a constant governed by the metasurface structure and P_c is the critical period, which leads to critical coupling of the radiative dipole and the in-plane diffractive modes. To illustrate the SHG efficiency as a function of the period, we plotted the maximum SH signal for different periodicities (Figure S.I.13). It is observed that below and above the critical period (P_c), the SH intensity scales as the 4th power of the period (P). This can be rationalized from our previous numerical analogy where the fundamental intensity (I_ω) scales quadratically (P^{-2}) above P_c. In a first approximation [45], the observed SH intensity is expected to scale quadratically with the fundamental field enhancement, thus demonstrating a quadratic dependency on the period ($I_{2\omega} \alpha\ I_\omega^2 \rightarrow I_{2\omega} \alpha\ P^{-4}$). From the simulation, it appears that the SH signal should be at least 8100 times. The discrepancy seen between the numerical simulation and experimental data (Figure 4) can have different origins. The total scattered SH far-field intensity is proportional to the perpendicular component of the electric field intensity ($E_z(r, \omega)$). To further analyze the perpendicular ($E_z(r, \omega)$) and parallel components ($E_y(r, \omega)$) of the electric field, we plotted the mode profiles as shown in Figure S.I.14. From such mode profile plots, the electric field appears to be significantly enhanced in the substrate plane (reaching an amplitude of 100), while the enhancement for the field amplitude normal to the substrate plane reaches about 12. It is difficult to separate the contributions of the in-plane and normal fields on the overall SH enhancement. In planar media, it is usually the normal field component that is assumed to play the dominant role in the nonlinear conversion mechanism [46], and the amplitude enhancement of about 10 observed in Figure S.I.14 could explain the measured 100× SH enhancement. The system under study is however far from a planar geometry and it is likely that the overall SH signal stems from a combination of in-plane and normal field components. Elucidating these mechanisms in detail would require polarization- and angle-resolved measurements, that are beyond the scope of this publication, which primary aim is to demonstrate a facile large area fabrication technique with full geometrical control. In the same experimental context, the detection of the SH signal in reflection mode might also be another cause for the discrepancy, since a non-negligible part of the SH wave can propagate in the forward direction and escape detection.

In any case, the experimental results clearly show the ability of our fabrication technique to produce efficient metasurfaces that yield both high SHG and tunable QF with a low FWHM.

4 Conclusions

In conclusion, with a simple process of nanoimprinting and dewetting, we developed a technique whereby optical properties of all-dielectric metasurfaces can be finely tuned whilst keeping the same original Si master. The tunability of the optical properties is possible by applying different pressures, leading to a controlled change in period. By a process of successive dewetting, increasing particle sizes were obtained, which in turn tuned the inter-particle gap. With this ability to control these two independent parameters, different optical modes with large QF were observed in a simple way without undergoing any hard lithographic steps. In particular, we have shown that by this programmable process, field enhancement could be increased up to 100 times. Such enhancement of field could give rise to SHG with a tailored FWHM using an amorphous structure. We have experimentally and numerically verified that the performance of SH intensity can be significantly improved by proper tuning the different optical modes in our metasurface. We demonstrated an SH conversion efficiency that is significantly larger compared to plasmonic metasurfaces and Silicon. Our approach could also be generally applied to III–V semiconductors in the ultra-violet (UV) or vacuum ultra-violet (VUV) regions, where sharp SH signals are required for bio-molecule sensing application. Such a general design approach could indeed pave the way for the fabrication of nonlinear meta-devices, fast optical switching, frequency conversion, and light-based communication.

References

[1] A. Arbabi, Y. Horie, M. Bagheri, and A. Faraon, "Dielectric metasurfaces for complete control of phase and polarization with subwavelength spatial resolution and high transmission," *Nat. Nanotechnol.*, vol. 10, pp. 937–943, 2015.

[2] D. G. Baranov, D. A. Zuev, S. I. Lepeshov, et al., "All-dielectric nanophotonics: the quest for better materials and fabrication techniques," *Optica*, vol. 4, p. 814, 2017.

[3] M. Decker and I. Staude, "Resonant dielectric nanostructures: a low-loss platform for functional nanophotonics," *J. Opt.*, vol. 18, p. 103001, 2016.

[4] M. Decker, I. Staude, M. Falkner, et al., "High-efficiency dielectric Huygens' surfaces," *Adv. Opt. Mater.*, vol. 3, pp. 813–820, 2015.

[5] N. Yu and F. Capasso, "Flat optics with designer metasurfaces," *Nat. Mater.*, vol. 13, pp. 139–150, 2014.

[6] B. Metzger, M. Hentschel, and H. Giessen, "Probing the near-field of second-harmonic light around plasmonic nanoantennas," *Nano Lett.*, vol. 17, pp. 1931–1937, 2017.

[7] D. Smirnova, A. I. Smirnov, and Y. S. Kivshar, "Multipolar second-harmonic generation by Mie-resonant dielectric nanoparticles," *Phys. Rev. A*, vol. 97, p. 013807, 2018.

[8] P. P. Vabishchevich, S. Liu, M. B. Sinclair, G. A. Keeler, G. M. Peake, and I. Brener, "Enhanced second-harmonic generation using broken symmetry III–V semiconductor fano metasurfaces," *ACS Photonics*, vol. 5, pp. 1685–1690, 2018.

[9] J. D. Sautter, L. Xu, A. E. Miroshnichenko, et al., "Tailoring second-harmonic emission from (111)-GaAs nanoantennas," *Nano Lett.*, vol. 19, pp. 3905–3911, 2019.

[10] S. V. Makarov, M. I. Petrov, U. Zywietz, et al., "Efficient second-harmonic generation in nanocrystalline silicon nanoparticles," *Nano Lett.*, vol. 17, pp. 3047–3053, 2017.

[11] J. Butet, P.-F. Brevet, and O. J. F. Martin, "Optical second harmonic generation in plasmonic nanostructures: from fundamental principles to advanced applications," *ACS Nano*, vol. 9, pp. 10545–10562, 2015.

[12] M. J. Huttunen, R. Czaplicki, and M. Kauranen, "Nonlinear plasmonic metasurfaces," *J. Nonlinear Opt. Phys. Mater.*, vol. 28, p. 1950001, 2019.

[13] M. Hentschel, B. Metzger, B. Knabe, K. Buse, and H. Giessen, "Linear and nonlinear optical properties of hybrid metallic-dielectric plasmonic nanoantennas," *Beilstein J. Nanotechnol.*, vol. 7, pp. 111–120, 2016.

[14] M. Parry, A. Komar, B. Hopkins, et al., "Active tuning of high-Q dielectric metasurfaces," *Appl. Phys. Lett.*, vol. 111, p. 053102, 2017.

[15] M. V. Rybin, K. L. Koshelev, Z. F. Sadrieva, et al., "High-Q supercavity modes in subwavelength dielectric resonators," *Phys. Rev. Lett.*, vol. 119, p. 243901, 2017.

[16] F. Wang, A. B. F. Martinson, and H. Harutyunyan, "Efficient nonlinear metasurface based on nonplanar plasmonic nanocavities," *ACS Photonics*, vol. 4, pp. 1188–1194, 2017.

[17] J. T. Collins, D. C. Hooper, A. G. Mark, C. Kuppe, and V. K. Valev, "Second-harmonic generation optical rotation solely attributable to chirality in plasmonic metasurfaces," *ACS Nano*, vol. 12, pp. 5445–5451, 2018.

[18] A. Hessel and A. A. Oliner, "A new theory of Wood's anomalies on optical gratings," *Appl. Opt.*, vol. 4, p. 1275, 1965.

[19] A. Maradudin, I. Simonsen, J. Polanco, and R. Fitzgerald, "Rayleigh and Wood anomalies in the diffraction of light from a perfectly conducting reflection grating," *J. Opt.*, vol. 18, p. 024004, 2016.

[20] D. C. Hooper, C. Kuppe, D. Wang, et al., "Second harmonic spectroscopy of surface lattice resonances," *Nano Lett.*, vol. 19, pp. 165–172, 2019.

[21] B. Gallinet, T. Siegfried, H. Sigg, P. Nordlander, and O. J. F. Martin, "Plasmonic radiance: probing structure at the Ångström Scale with visible light," *Nano Lett.*, vol. 13, pp. 497–503, 2013.

[22] Y. Chu and K. B. Crozier, "Experimental study of the interaction between localized and propagating surface plasmons," *Opt. Lett.*, vol. 34, p. 244, 2009.

[23] B. Gallinet and O. J. F. Martin, "Refractive index sensing with subradiant modes: a framework to reduce losses in plasmonic nanostructures," *ACS Nano*, vol. 7, pp. 6978–6987, 2013.

[24] A. Christ, Y. Ekinci, H. H. Solak, N. A. Gippius, S. G. Tikhodeev, and O. J. F. Martin, "Controlling the Fano interference in a plasmonic lattice," *Phys. Rev. B Condens. Matter*, vol. 76, p. 201405, 2007.

[25] P. Törmä and W. L. Barnes, "Strong coupling between surface plasmon polaritons and emitters: a review," *Rep. Prog. Phys.*, vol. 78, p. 013901, 2015.

[26] L. Michaeli, S. Keren-Zur, O. Avayu, H. Suchowski, and T. Ellenbogen, "Nonlinear surface lattice resonance in plasmonic nanoparticle arrays," *Phys. Rev. Lett.*, vol. 118, p. 243904, 2017.

[27] R. Czaplicki, A. Kiviniemi, M. J. Huttunen, et al., "Less is more: enhancement of second-harmonic generation from metasurfaces by reduced nanoparticle density," *Nano Lett.*, vol. 18, pp. 7709–7714, 2018.

[28] A. Kiselev, G. D. Bernasconi, and O. J. F. Martin, "Modes interplay and dynamics in the second harmonic generation of plasmonic nanostructures," *Opt. Express*, vol. 27, p. 38708, 2019.

[29] M. H. Lee, M. D. Huntington, W. Zhou, J.-C. Yang, and T. W. Odom, "Programmable soft lithography: solvent-assisted nanoscale embossing," *Nano Lett.*, vol. 11, pp. 311–315, 2011.

[30] L. Liu, J. Zhang, M. A. Badshah, et al., "A programmable nanoreplica molding for the fabrication of nanophotonic devices," *Sci. Rep.*, vol. 6, p. 22445, 2016.

[31] A. Yang, A. J. Hryn, M. R. Bourgeois, et al., "Programmable and reversible plasmon mode engineering," *Proc. Natl. Acad. Sci. USA*, vol. 113, pp. 14201–14206, 2016.

[32] B. J. Eggleton, B. Luther-Davies, and K. Richardson, "Chalcogenide photonics," *Nat. Photonics*, vol. 5, pp. 141–148, 2011.

[33] H. Lin, Y. Song, Y. Huang, et al., "Chalcogenide glass-on-graphene photonics," *Nat. Photonics*, vol. 11, pp. 798–805, 2017.

[34] W. Yan, T. Nguyen-Dang, C. Cayron, et al., "Microstructure tailoring of selenium-core multimaterial optoelectronic fibers," *Opt. Mater. Express*, vol. 7, p. 1388, 2017.

[35] W. Yan, Y. Qu, T. Das Gupta, et al., "Semiconducting nanowire-based optoelectronic fibers," *Adv. Mater.*, vol. 29, p. 1700681, 2017.

[36] Y. Zou, L. Moreel, H. Lin, et al., "Solution processing and resist-free nanoimprint fabrication of thin film chalcogenide glass devices: inorganic-organic hybrid photonic integration," *Adv. Opt. Mater.*, vol. 2, pp. 759–764, 2014.

[37] M. Guignard, V. Nazabal, J. Troles, et al., "Second-harmonic generation of thermally poled chalcogenide glass," *Opt. Express*, vol. 13, p. 789, 2005.

[38] C. R. Ma, J. H. Yan, Y. M. Wei, and G. W. Yang, "Second harmonic generation from an individual amorphous selenium nanosphere," *Nanotechnology*, vol. 27, p. 425206, 2016.

[39] T. Das Gupta, L. Martin-Monier, W. Yan, et al., "Self-assembly of nanostructured glass metasurfaces via templated fluid instabilities," *Nat. Nanotechnol.*, vol. 14, pp. 320–327, 2019.

[40] N. Sultanova, S. Kasarova, and I. Nikolov, "Dispersion properties of optical polymers," *Acta Phys. Polonica A Polish Acad. Sci.*, vol. 116, pp. 585–587, 2009.

[41] C. Readman, B. De Nijs, I. Szabó, et al., "Anomalously large spectral shifts near the quantum tunnelling limit in plasmonic rulers with subatomic resolution," *Nano Lett.*, vol. 19, pp. 2051–2058, 2019.

[42] A. Manjavacas, L. Zundel, and S. Sanders, "Analysis of the limits of the near-field produced by nanoparticle arrays," *ACS Nano*, vol. 13, pp. 10682–10693, 2019.

[43] K. Y. Yang, J. Butet, C. Yan, G. D. Bernasconi, and O. J. F. Martin, "Enhancement mechanisms of the second harmonic generation from double resonant aluminum nanostructures," *ACS Photonics*, vol. 4, pp. 1522–1530, 2017.

[44] K. Koshelev, Y. Tang, K. Li, D.-Y. Choi, G. Li, and Y. Kivshar, "Nonlinear metasurfaces governed by bound states in the continuum," *ACS Photonics*, vol. 6, pp. 1639–1644, 2019.

[45] J. Wang, J. Butet, A.-L. Baudrion, et al., "Direct comparison of second harmonic generation and two-photon photoluminescence from single connected gold nanodimers," *J. Phys. Chem. C*, vol. 120, pp. 17699–17710, 2016.

[46] F. X. Wang, F. J. Rodríguez, W. M. Albers, R. Ahorinta, J. E. Sipe, and M. Kauranen, "Surface and bulk contributions to the second-order nonlinear optical response of a gold film," *Phys. Rev. B*, vol. 80, p. 233402, 2009.